



HAL
open science

Comparison of the phase-field approach and cohesive element modeling to analyze the double cleavage drilled compression fracture test of an elastoplastic material

Arnaud Coq, Julie Diani, Stella Brach

► To cite this version:

Arnaud Coq, Julie Diani, Stella Brach. Comparison of the phase-field approach and cohesive element modeling to analyze the double cleavage drilled compression fracture test of an elastoplastic material. *International Journal of Fracture*, 2024, 10.1007/s10704-023-00755-2 . hal-04412583

HAL Id: hal-04412583

<https://hal.science/hal-04412583v1>

Submitted on 23 Jan 2024

HAL is a multi-disciplinary open access archive for the deposit and dissemination of scientific research documents, whether they are published or not. The documents may come from teaching and research institutions in France or abroad, or from public or private research centers.

L'archive ouverte pluridisciplinaire **HAL**, est destinée au dépôt et à la diffusion de documents scientifiques de niveau recherche, publiés ou non, émanant des établissements d'enseignement et de recherche français ou étrangers, des laboratoires publics ou privés.

Comparison of the phase-field approach and cohesive element modeling to analyze the double cleavage drilled compression fracture test of an elastoplastic material

Arnaud Coq¹ Julie Diani¹ Stella Brach²

¹ Laboratoire de mécanique des solides, UMR 7649 CNRS, Ecole Polytechnique, Route de Saclay, 91128 Palaiseau, France

² IBM Zurich Research Laboratory, Säumerstrasse 4, CH-8803 Rüschlikon, Switzerland December 15, 2023

Abstract

Brittle material Mode I fracture may be characterized by the double cleavage drilled compression test. For linear elastic materials, the critical energy release rate, or fracture toughness, can be estimated simply using the linear elastic fracture mechanics. For other types of constitutive behavior, the material parameter has to be determined with numerical fracture modeling. In this paper, we have used two approaches, the phase-field damage and the cohesive elements, in order to estimate the critical energy release rate of an elastoplastic material. Firstly, we assessed the numerical models and discussed their parameters by comparison of available data from double cleavage drilled compression experimental tests run on a silica glass. Both phase-field damage and cohesive zone models were able to reproduce fracture initiation at the observed macroscopic stress for the linear elastic material. However, the material toughness could not be predicted by the phase-field approach due to the result dependence on the model regularization parameter. Secondly, an elastoplastic methyl methacrylate polymer was submitted to the compression test in our lab. Both models were then extended for elastic-perfectly plastic materials. Crack initiation was obtained at the observed macroscopic strain for similar critical energy release rate ranges for both approaches, providing good confidence in the estimated material toughness.¹

keywords: Phase-field; Cohesive elements; Fracture mechanics; Compression; Elastoplasticity

¹Preprint - Accepted 2024

1 Introduction

The double cleavage drilled compression (DCDC) test [1] characterizes well Mode I fracture of brittle materials such as glasses [2]. It consists in submitting to quasi-static uniaxial compression, a slender parallelepiped with a circular hole at its center and vertical pre-cracks at the poles of the hole. The material critical energy release rate, G_c , may be estimated by linear elastic fracture mechanics (LEFM) analysis [2, 3, 4, 5, 6]. The test has been later extended to other materials such as plaster [7] and glassy polymers [8, 9, 10]. According to the temperature and the applied strain rate, polymers may show viscoelasticity, elastoplasticity or viscoplasticity. In such cases, the LEFM analysis no longer applies. Therefore, the present contribution aims at proposing numerical analyses of the DCDC tests that could be applied beyond linear elasticity. The phase-field approach and the cohesive zone model (CZM) have been chosen for their ease of implementation. On one hand, the phase-field approach, based on energy minimization, presents the advantage of not requiring a predefined crack path. On the other hand, the CZM is ready to use in several commercial finite element softwares. For comparison purpose, experimental data obtained on a linear elastic material have been collected from the literature [2], and tests have been carried out on an acrylate polymer displaying elastoplasticity.

The phase-field modeling of fracture [11] is a variational approach of Griffith's energy balance theory. The numerical method, as regularized by [12], has quickly drawn positive attention for its lack of specific meshing requirement and its ease of implementation. It has been successfully applied for various elastic problems ([13, 14] among others), and later extended theoretically to the case of plasticity [15, 16, 17, 18]. However, the DCDC test brings an additional difficulty since most of the specimen is in compression, and the performance of the phase-field original formulation remains questionable for such loading conditions [14]. Few studies [7, 19] have modeled the DCDC test with this approach. They have reproduced experiments to some level, in the context of linear elasticity only.

The cohesive zone model [20] has been introduced to account for the separation of two surfaces. Using finite element analysis, cohesive elements are added along the expected crack path. These elements satisfy to stress-displacement laws per se introducing a length scale in the constitutive equations. As both surfaces separate, the elements soften and ultimately break. The cohesive elements have been successfully applied for homogeneous and heterogeneous materials [21] in elasticity [22] as well as plasticity [23]². Cohesive elements have already been applied once to model the DCDC test with an orthorhombic hole in the case of linear elasticity [24]. While no comparison with experiments was shown, a positive comparison with the coupled criterion [25] was proposed. Therefore, a quantitative comparison of the CZM approach for DCDC experiments in linear elasticity as well as in elastoplasticity is still missing. Finally, the quantitative comparison of both modeling approaches confronted with actual experimental

²Note that only a few contributions are cited here among the vast literature on CZM

results remains to be done.

The paper is organized as follows. Next section presents the DCDC test and the experimental results obtained on an elastoplastic methyl methacrylate polymer. Section 3 introduces the theoretical and numerical aspects of both modeling approaches as used. Firstly, the fracture models are applied in linear elasticity and confronted to data from the literature. Secondly, the models are used to assess the critical energy release rate of the tested elastoplastic acrylate.

2 Mode I fracture DCDC test

2.1 Test and LEFM analysis

In the double cleavage drilled compression test, a slender parallelepiped with a circular hole at its center is submitted to a compression loading along its long direction (Figure 1). Two pre-cracks made at the poles of the hole are then submitted to Mode I opening. By following the crack propagation with respect to the applied macroscopic compression stress, one may estimate the material Mode I critical energy release rate.

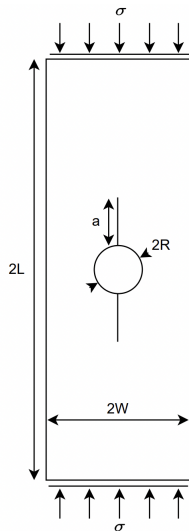


Figure 1: Illustration of the DCDC test.

For linear elastic materials, DCDC test fracture mechanics analysis has been carried out with finite elements [3, 5] and analytical [9] models. Expressions of the stress intensity factor K , or equivalently the strain energy release rate G , have been proposed as functions of the applied compression stress σ and of the sample geometry quantities, $\frac{W}{R}$ and $\frac{a}{R}$, with $2W$ the sample width, R the hole radius and a the current crack length. The critical value G_c is defined as the

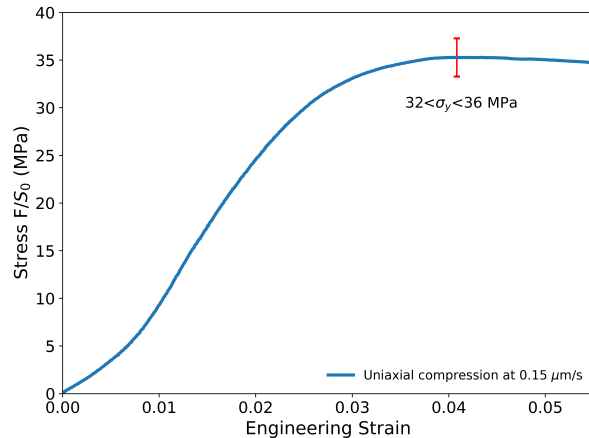


Figure 2: Monotonic uniaxial compression stress with respect to the compression strain applied at a constant crosshead speed of $0.15 \mu\text{m/s}$ measured on a solid cylinder sample.

value of G at which the crack propagates. The LEFM framework has been successfully applied to DCDC experiments on glasses [2]. However, this test has been extended to polymers [10], which rarely show linear elasticity, as next section will illustrate, and for which the LEFM analysis may lead to large errors.

2.2 DCDC test run on an elastoplastic polymer

The material used is a methyl methacrylate (MMA) manufactured by Bostik with a glass transition temperature of $100 \text{ }^\circ\text{C}$ that is used for joint applications.

First monotonic compression tests were run on solid cylinders of 15 mm height and 8 mm diameter at quasi-static $0.15 \mu\text{m/s}$ constant crosshead speed (approximate constant strain rate of 10^{-5} s^{-1} like for the DCDC test). This test was performed using digital image correlation to observe the local strain on a speckled flat surface measuring 4 mm in width. The experimental set-up, involving a CCD camera and multi-axis mounting, is detailed in [26, 27]. Figure 2 illustrates the elastoplastic stress-strain response of the material with an uncertainty on the yield stress determined by three tests.

Sample mold dimensions were $2L \times 2W$ equal to $50 \times 12 \text{ mm}^2$, 5.3 mm thickness, and a central hole of 1.5 mm of radius. A diamond wire of 0.3 mm diameter was used to cut the vertical pre-notches at the poles of the circular hole. The verticality of the pre-notches was satisfied within a 2° angle tolerance.

The DCDC compression tests were conducted on a conventional Instron tensile machine and images of the crack tip were recorded with a JAI SP 20000 camera equipped with a telecentric lens. A two-plane plexiglass setup was used to prevent any out-of-plane displacement and friction was prevented by adding a silicone lubricant. The compression loading has been applied at a low constant

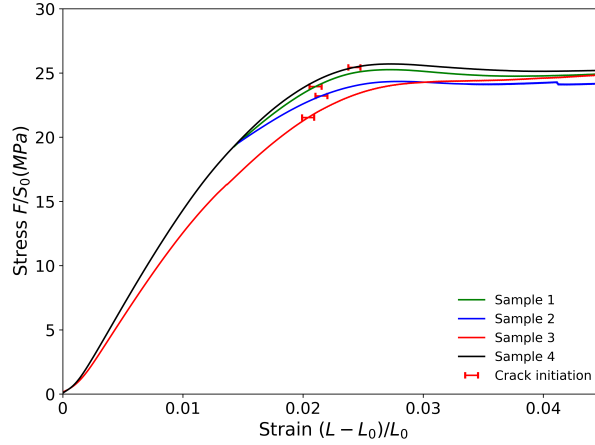


Figure 3: Macroscopic compression stress with respect to the applied compression strain recorded during the DCDC test. The red bars show the onset of the crack propagation and represent the uncertainty of the measure.

crosshead speed of $0.5 \mu\text{m/s}$ (approximately constant strain rate of 10^{-5}s^{-1}). Figure 3 shows the macroscopic compression stress with respect to applied compression strain. The red bars show the onset of the crack propagation and its uncertainty, which has been observed at a macroscopic strain of 0.0215 ± 0.0015 on four samples.

The material was transparent enough to estimate the crack length with respect to the applied macroscopic strain by simple image post-processing with Fiji [28]. As shown in Figure 3, the crack initiates as the material becomes plastic and the macroscopic stress remains close to constant during the propagation. Figure 4 illustrates how the crack length increases with the applied macroscopic strain. Cavities appear in front of the notches and nucleate to create sharper cracks only at the onset of propagation. Then, both cracks progress continuously and similarly as the load increases.

Next section presents how the DCDC test will be modeled by the phase-field approach and the cohesive elements.

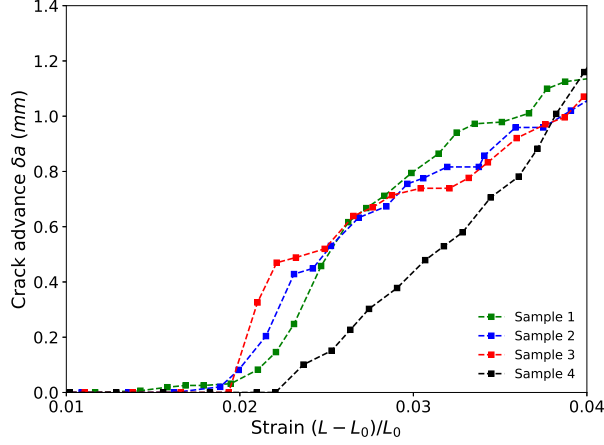


Figure 4: DCDC test - Crack advance length normalized by the hole radius with respect to the applied macroscopic strain for three specimens.

3 Phase-field approach and cohesive element modeling

3.1 Phase-field approach for DCDC test

3.1.1 Linear elastic behavior

In the variational approach developed in [11, 12, 29], the fracture problem is solved by finding the displacement field \underline{u}^* and the damage field d^* satisfying,

$$(\underline{u}^*, d^*)_\ell = \underset{\substack{\underline{u} \in \mathcal{U}_{ad} \\ d \geq 0}}{\operatorname{argmin}} \xi_\ell(\underline{u}, d) \quad (1)$$

with \mathcal{U}_{ad} the set of kinematically-admissible displacement fields, and under the damage irreversibility condition $d \geq 0$. We consider here a linear elastic solid Ω , characterized by its stiffness tensor \mathbb{C} and critical energy release rate G_c . The regularized total energy ξ_ℓ , sum of the stored elastic energy density and of the fracture energy density, writes as,

$$\begin{cases} \xi_\ell(\underline{u}, d) = \int_{\Omega} (W^{el} + W^{frac}) d\Omega \\ W^{el} = \frac{1}{2} \underline{\underline{\epsilon}} : (1 - d)^2 \mathbb{C} : \underline{\underline{\epsilon}}, & W^{frac} = \frac{3G_c}{8} \left(\frac{d}{\ell} + \ell |\nabla d|^2 \right), \end{cases} \quad (2)$$

with strain tensor $\underline{\underline{\epsilon}} = \frac{1}{2} (\nabla \underline{u} + \nabla \underline{u}^T)$. The length ℓ is a positive and small regularization parameter.

Phase-field modeling of compressive tests leads to difficulties that are usually circumvented by selectively coupling parts of the strain energy density with the

damage variable [14]. For instance, the following decomposition for isotropic materials, was introduced [30] to prevent crack nucleation under pure compression:

$$\begin{aligned}
W^{el} &= \frac{B}{2} tr^2(\underline{\underline{\epsilon}}^-) + (1-d)^2 \left(\frac{B}{2} tr^2(\underline{\underline{\epsilon}}^+) + \mu (\underline{\underline{\epsilon}}_d : \underline{\underline{\epsilon}}_d) \right), \\
tr(\underline{\underline{\epsilon}}^+) &= \begin{cases} tr(\underline{\underline{\epsilon}}) & \text{if } tr(\underline{\underline{\epsilon}}) \geq 0, \\ 0, & \text{else if,} \end{cases} \\
tr(\underline{\underline{\epsilon}}^-) &= tr(\underline{\underline{\epsilon}}) - tr(\underline{\underline{\epsilon}}^+),
\end{aligned} \tag{3}$$

with μ the shear modulus, B the bulk modulus, and $\underline{\underline{\epsilon}}_d$ the deviatoric part of the strain tensor. For the DCDC test, the use of such a decomposition introduces unrealistic damage at the equator of the poles before the crack starts propagating along the main axis of the specimen [19]. Therefore, [19] proposed to use other energy decompositions such as the tension/compression decomposition from [31] and an orthogonal decomposition. A fourth decomposition was used by [32] in the case of anisotropic fracture properties. The major drawback of using a specific energy decomposition to reproduce a chosen test is that it may generate a dependence of the material parameter G_c to the decomposition, the structure geometry, or the applied loading.

One other possible approach is to keep the decomposition introduced in Eq. (3) and limit the domain of possible crack propagation. This can be done by preventing the material to be damaged in some areas. It is known from prior knowledge and experimental observations that crack initiation is expected to occur at the pre-crack tip under the current loading conditions and geometry. By preventing damage at the equator of the circular hole, we can observe damage concentrating at the pre-crack tip as observed experimentally. It is important to note that this damage restriction approach is applicable in cases where the initiation location and the crack path are already known. Nevertheless, it is crucial to acknowledge that crack nucleation, in general, remains an ongoing topic of debate within the phase-field community [33, 34]. While there are situations where the loading conditions and geometry may suggest likely nucleation locations, predicting crack nucleation accurately requires further investigation and research. It is important to note that the focus of the current study does not specifically address crack nucleation location. Hence, considering the specific knowledge we have about initiation and propagation locations for the DCDC test, we have chosen the second option limiting the damage area to evaluate the critical energy release rate.

Equation (1) is conventionally solved by an iterative minimization scheme, that finds local minimums of \underline{u} and d alternatively until convergence is achieved [14]. The model has been implemented in finite elements by using the open-source library Fenics [35]. The minimization of energy with respect to \underline{u} is linear, and is solved using the parallel sparse direct solver MUMPS. The constrained energy minimization with respect to d is solved using PETSC TAO bound constrained solver. Meshes were generated by mesh generator Gmsh [36] using an

unstructured Frontal-Delaunay algorithm with a target element length of $\ell/5$ in the propagation area (where d evolves).

3.1.2 Elastoplasticity

The original variational formulation was extended to elastoplasticity in several studies [14, 15, 17, 31, 37]. The current paper uses the approach developed by [14, 17, 37]. The material is considered elastic-perfectly plastic satisfying to the von Mises yield criterion $\sqrt{\frac{3}{2}\underline{\underline{s}} : \underline{\underline{s}}} \leq \sigma_y$, with $\underline{\underline{s}}$ the deviatoric part of the Cauchy stress tensor. The minimization problem now reads as:

$$(\underline{\underline{u}}^*, \underline{\underline{\epsilon}}_p^*, d^*)_\ell = \underset{\substack{\underline{\underline{u}} \in \mathcal{U}_{ad}, \underline{\underline{\epsilon}}_p \in \mathcal{G}, \\ d \geq 0}}{\arg \min} \xi_\ell(\underline{\underline{u}}, \underline{\underline{\epsilon}}_p, d) \quad (4)$$

with \mathcal{G} is the set of plastically-incompressible strain rates. The total energy density to minimize writes as,

$$\begin{aligned} \xi_\ell(\underline{\underline{u}}, \underline{\underline{\epsilon}}_p, d) &= \int_\Omega \frac{1}{2} (\underline{\underline{\epsilon}} - \underline{\underline{\epsilon}}_p) : (1-d)^2 \mathbb{C} : (\underline{\underline{\epsilon}} - \underline{\underline{\epsilon}}_p) d\Omega \\ &+ \int_\Omega b(d) \sqrt{\frac{2}{3}} \sigma_y \bar{p} d\Omega + \int_\Omega \frac{3G_c}{8} \left(\frac{d}{\ell} + \ell |\nabla d|^2 \right) d\Omega, \end{aligned} \quad (5)$$

with \bar{p} the cumulative plastic strain. The function $b(d)$, generally defined as $(1-d)^2$, is a second damage-dependent degradation function. Finally, the plastic incompressibility condition is ensured by penalization.

At each time-step t^i , firstly, the functional ξ_ℓ is minimized by finding the optimal kinematically-admissible displacement $\underline{\underline{u}}^i$ and plastically-admissible strain $\underline{\underline{\epsilon}}_p^i$ while keeping the damage variable d^{i-1} constant. The cumulative plasticity is computed as $\bar{p}_i = \bar{p}_{i-1} + \|\underline{\underline{\epsilon}}_p^i - \underline{\underline{\epsilon}}_p^{i-1}\|$. Secondly, ξ_ℓ is minimized with respect to d while keeping $\underline{\underline{u}}^i$ and $\underline{\underline{\epsilon}}_p^i$ constant. The second minimization accounts for the damage irreversibility constraint. This process is repeated iteratively until convergence is achieved. The energy minimization with respect to $\underline{\underline{\epsilon}}_p$ is solved using the SNES PETSC solver with a line search technique.

3.2 Cohesive zone model

The basis of the theory [20] is to consider a traction-separation law between two surfaces. The law accounts for the strength and toughness of the cohesive forces taking place at the interface. As the surfaces separate, the cohesive forces soften and ultimately go to zero when the interface breaks.

For simplicity purpose, we consider a triangular traction-separation law, for which the stress T with respect to the surface separation displacement, δ , is defined by three parameters only as illustrated in Figure 5.³ The cohesive

³The interested reader will find in [24], a study on the impact of the shape of the damage function for the DCDC test.

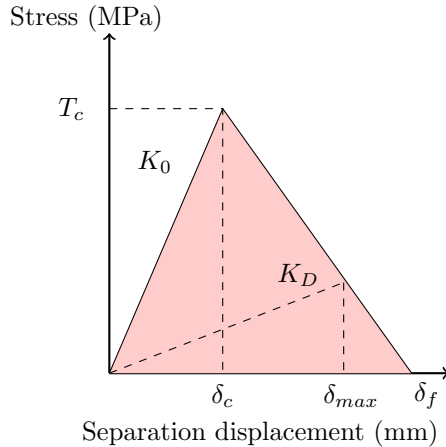


Figure 5: Illustrations of the cohesive traction-separation law.

element has an initial stiffness of K_0 constant as long as the stress holds below T_c . Once the critical stress T_c is reached, the cohesive element stiffness becomes $K_D = (1 - D)K_0$, with D a damage parameter. In the case of linear damage (Figure 5), D may write as,

$$D = \frac{\delta_f(\delta_{max} - \delta_c)}{\delta_{max}(\delta_f - \delta_c)}, \quad (6)$$

with δ_c the displacement at damage initiation, δ_f the displacement at failure and δ_{max} the maximum separation before break.

The traction-separation law in Figure 5 may be considered for the surface normal displacement (fracture opening Mode) as well as for the tangential displacement, which accounts for surface separation due to shearing or equivalently fracture sliding Modes. When tangential displacements are considered δ in Eq. (6) may write as,

$$\delta = \sqrt{\langle \delta_n \rangle^2 + \delta_t^2 + \delta_s^2} \quad (7)$$

where δ_t and δ_s are the tangential displacements (in three dimensions) and $\langle \cdot \rangle$ are the Macauley brackets allowing to distinguish normal separation from normal compression.

Abaqus finite element code [38] was chosen for the simulations. Considering the dimensions of the geometry and the generally required refinement for CZM elements [39], 2D calculations have been run using cohesive quads elements COH2D4 that have zero thicknesses.

Several choices of damage evolution and criterion are possible. We have considered both tangent and normal traction-separation laws with the same parameters. However, one may neglect the tangent separation law like in [24], since as expected the damage occurs due to Mode I surface opening. We chose to initiate

damage as soon as either the normal or the tangential stress reaches its critical values, T_c (Abaqus MAXS criterion). The linear damage evolution Eq. (6) is governed by the maximum displacement δ_f , which writes as `*DAMAGE EVOLUTION, TYPE=DISPLACEMENT, SOFTENING=LINEAR`. Therefore, numerical results may be discussed with respect to the three cohesive element parameters K_0 , T_c and δ_f or equivalently K_0 , T_c and G_c since the energy consumed by the break of an element, $\frac{T_c \times \delta_f}{2}$, is the critical fracture energy released rate G_c .

In order to estimate the load at crack initiation accurately, it is typical to consider several cohesive elements to cover the length of the cohesive process zone, l_{cz} , which may be approximated by $l_{cz} \approx ME \frac{G_c}{T_c^2}$ [39] for linear elastic materials, with M depending on the model and the geometry of the sample for slender structures. Note that in our case, M is unknown and may be significantly smaller than one. Moreover, there is no strict number of elements required over the cohesive zone length, therefore this number should be chosen large enough to keep the results unchanged by further refinement but small enough to limit the duration of calculations. Finally, a regular mesh is recommended along the cohesive surfaces to avoid damage appearance in unrealistic locations due to undesired mesh irregularities.

4 Model results for the DCDC test on a linear elastic material

In order to compare both modeling approaches, we first consider the experimental results from [2] on DCDC test performed on brittle fused silica. Specimens of dimensions, length $2L = 75$ mm, width $2W = 7.5$ mm, thickness $D = 6.5$ mm, and hole radius $R = 1.0$ mm with initial cracks of lengths $a = 2.0$ mm have been submitted to quasi-static compression loadings. Values of the applied compression stress with respect to the crack progress, reported in Table 1 of [2] will be used for model comparison. As reported by the authors, crack propagation in fused silica DCB geometry shows a value of critical stress intensity factor $K_{Ic} = 0.74$ MPa.m^{1/2} [40]. They performed a LEFM analysis of the DCDC test by running finite element plane stress simulations on the same geometry with various crack lengths, and reached the same value of K_{Ic} within a range of 10%, for input material parameters $E = 68974$ MPa and $\nu = 0.16$ for the Young modulus and Poisson's ratio. The corresponding critical energy release rate value useful for the simulations coming next is $G_c = 7.9 \cdot 10^{-3}$ MPa.mm.

4.1 Phase-field simulations

The top half of the DCDC specimen (Figure 1) was modeled and symmetry conditions were applied at the bottom. The mesh was refined around the hole and along a vertical strip enclosing the pre-crack (Figure 6). The width of the strip where the damage is allowed to evolve is represented by the mesh

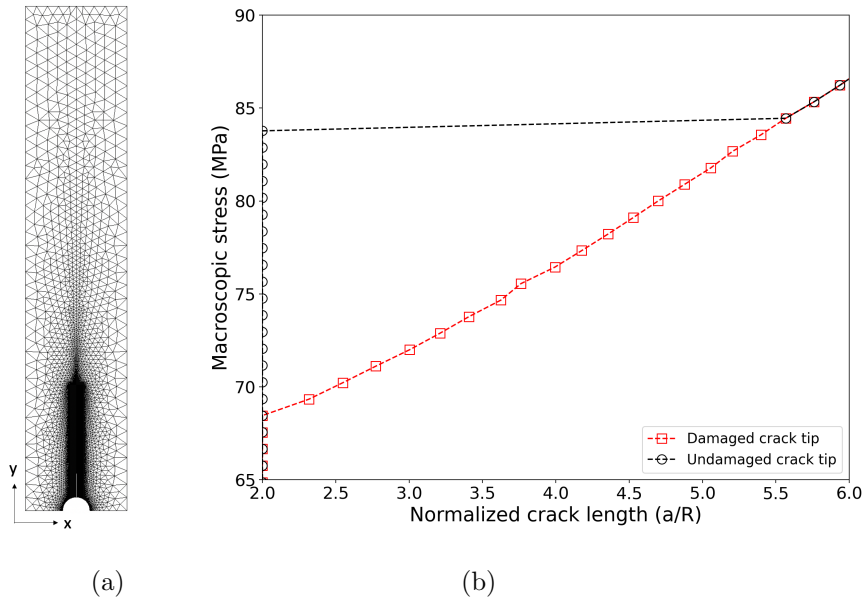


Figure 6: (a) Illustration of the finite element mesh refinement. (b) Crack length vs. macroscopic stress for a damaged and undamaged crack tip.

refinement. Simulations were performed in 2D with plane stress assumption. The damage variable d was set to one on the edges of the tip of the pre-crack.

A compressive displacement was applied at the top of the structure, with a step increment of $5 \cdot 10^{-4}$ mm. The crack length is initially equal to the pre-crack length and then evaluated as the maximum distance from the pole of the hole at which the damage d reaches the value one. During the loading, the sample first behaves elastically, then at a given stress, the crack length increases linearly with the macroscopic stress (Figure 6). Note that setting d equal to one at the crack tip is essential in the accurate evaluation of the stress at crack initiation. As a matter of fact, we observed that without pre-damage at the crack tip, the stress at initiation is significantly overestimated as shown in Figure 6.

To lower the numerical cost of the simulations while preserving good accuracy, two areas have been defined with different mesh sizes. Far from the crack, the mesh size was set to a coarse value of $M_s = 0.1$ mm, while a finer mesh size $m_s = \frac{\ell}{5}$ is prescribed in the crack propagation vicinity.

We first assessed the impact of the regularization length ℓ on the numerical results. We remind that when minimizing Eq. (2), the crack propagates when the strain energy release rate reaches the numerical value $G_c^{num} = G_c(1 + \frac{3m_s}{8\ell})$ [29]. Therefore, the model parameter G_c^{num} was set at the experimental toughness value $7.9 \cdot 10^{-3}$ MPa.mm. The obtained crack length with respect to the resulting compressive stress is shown in Figure 7 for several values of ℓ . Note that as ℓ decreases, the numerical results converge toward the experimental one.

The parameter ℓ is shown to have a significant impact on the stress value at crack initiation. In the literature, some authors ([30, 14, 7] for instance) chose to relate ℓ to the ultimate strength of an undamaged bar submitted to a uniaxial tension test. In our case, the value $\ell = 0.002$ mm, giving satisfactory results for the DCDC test, corresponds to a stress at break of 308 MPa, which does not match the values between 50 and 110 MPa that may be found in the literature for similar materials. Finally, as shown in Figure 7, when setting $\ell = 0.05$ mm, corresponding to a reasonable value of ultimate strength of 68 MPa for the bar in uniaxial tension, G_c had to be increased by about 35% to reproduce the experimental data. We observe that the model relationship between the ultimate strength σ_c , the critical energy release rate G_c and ℓ , which writes as,

$$\ell = \frac{3G_c E}{8\sigma_c^2} \quad (8)$$

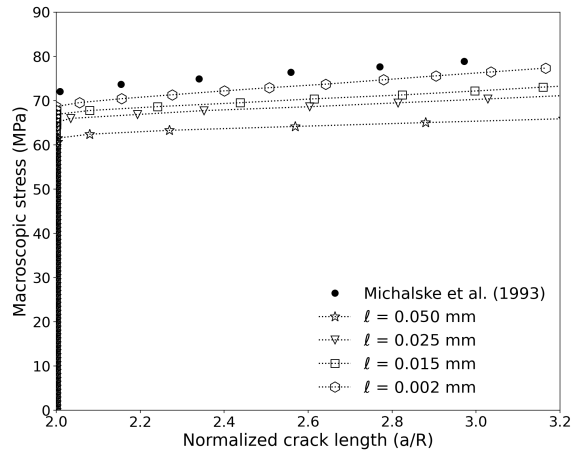
does not apply here. Consequently, in the current study, G_c is regarded as a material parameter while ℓ is a numerical parameter not necessarily linked to the physics of the material.

Next section, we evaluate how cohesive elements perform on the same problem.

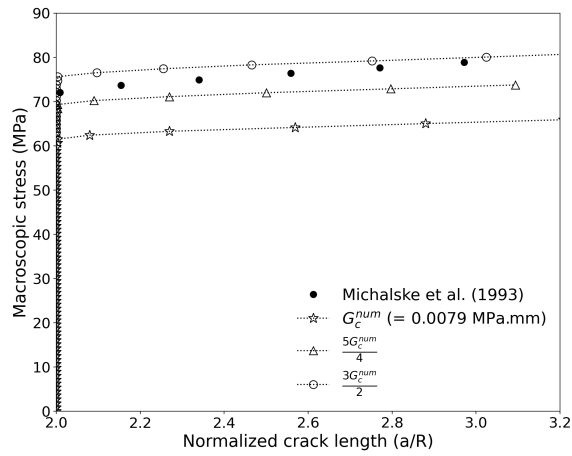
4.2 Cohesive element results

An analysis of the required cohesive mesh size and initial stiffness K_0 , has been performed. The top half of the 2D geometry was meshed adding cohesive elements of 0.03 to 5 microns along the crack path. It was found that 1 micron was adequate to observe cohesive element break for the material parameter ranges that have been explored. The initial stiffness of the cohesive elements, K_0 , should not modify the material response before damage. Based on this mechanical consideration, a rule of thumb has been proposed by [39] which writes in our case as, $\frac{WK_0}{E} \gg 1$, and which has been used as a first guideline. However, a compression test on the linear elastic geometry without cohesive elements has served as a reference case to possibly reject values of K_0 . Several values of K_0 from 7.10^6 to 7.10^8 MPa/mm were satisfactorily tested regarding the former criterion. While, as in [24], it was observed that the macroscopic stress at crack initiation decreases as the initial stiffness K_0 increases to finally reach a plateau, it was also observed that the number of time steps, required to reach the damage convergence, increases significantly as K_0 increases. In the end, the stiffness of $K_0 = 7.10^7$ MPa/mm was chosen to provide enough accuracy and to allow testing several material parameters. A maximum macroscopic compression strain of 0.003 was applied with a maximum strain step of 5.10^{-7} .

The impact of cohesive the parameters $G_c = \frac{T_c \times \delta_f}{2}$ and T_c are presented in Figure 8. First, simulations have been run with the experimental critical energy released rate $G_c = 0.0079$ MPa.mm provided by [2], and varying the critical stress T_c . It is shown that very satisfactory results are obtained for a range of reasonable values of critical strength. As a result, the crack advance is mostly driven by G_c . One notes in Figure 8 that the macroscopic stress at propagation



(a)



(b)

Figure 7: Phase-field fracture modeling of DCDC test [2]. (a) Impact of regularization parameter ℓ for material constant G_c [2]. (b) Impact of G_c for constant regularization parameter $\ell = 0.05$ mm.

varies significantly with G_c . Therefore, the critical energy release rate may be evaluated rather accurately.

In the end, both models have been able to reproduce the experimental results. However, we note that if unknown, the critical energy release rate could be evaluated by the CZM model only. The elastoplastic case is now addressed by comparing both modeling approaches to our experimental data obtained on the glassy MMA polymer in section 2.2.

5 DCDC analysis for a viscoplastic polymer

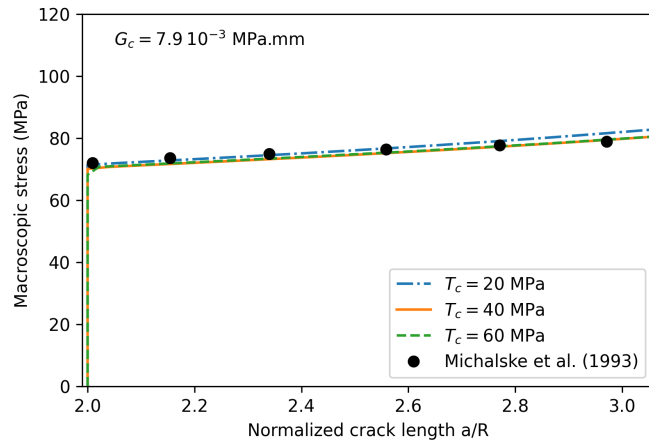
The compression response of the MMA (Figure 2) may be fairly approximated by an elastic-perfectly plastic behavior with a Young modulus of 1400 MPa, Poisson’s ratio of 0.4 and yield stress of 34 MPa. The exact geometry of one of the DCDC samples was reproduced with $L = 23.5$ mm, $W = 5.8$ mm, $R = 1.5$ mm, and $a = 3.15$ mm. Finally, plane stress 2D simulations have been run for both modeling approaches. The finite element macroscopic stress-strain curve compares well to the experimental results as shown in Figure 9. Due to the plastic plateau, the initiation of the crack propagation will be examined with respect to the applied compressive strain.

5.1 Phase-field approach results

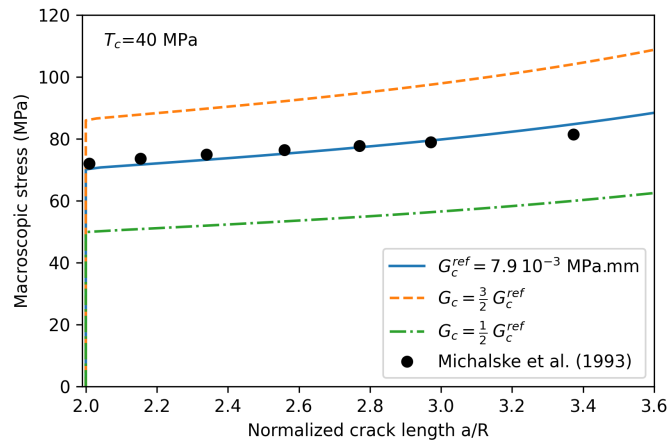
Only half of the specimen has been considered, and symmetry conditions applied at the boundary, mesh parameters M_s were set to 0.5 mm and $m_s = \ell/5$. Initial full damage, $d = 1$, was enforced at the crack tip. The compression strain at crack initiation is determined according to the minimization parameters ℓ and G_c .

First, the impact of regularization parameter ℓ , while keeping G_c^{num} constant, is presented in Figure 10a. For the tested values of ℓ , the damage propagation starts for the same macroscopic strain. Consequently, a fixed value of $\ell = 0.1$ mm was chosen to explore the effect of G_c . As G_c increases the required macroscopic strain to witness crack initiation increases (Figure 10b). Moreover, the experimental test is well reproduced when G_c varies between 0.30 and 0.35 MPa.mm.

Figure 11 displays how the damage evolves at the crack tip. It progresses along a vertical line without reaching the value one, usual sign of complete failure of the material. Meanwhile, the plasticity that develops along the damage path remains localized in a narrow area (Figure 12). The global changes of the elastic, plastic, and fracture energies with respect to the macroscopic applied displacement shown in Figure 13, helps recognize the initiation of the fracture well identified by the change of slope of the fracture energy. Moreover, the smooth increase of the latter highlights a constant propagation rate. This result is in good qualitative agreement with our experimental observations, once the pre-notch becomes a sharp crack. A comparison with experimental propagation rate in Figure 4 can’t be obtained as the failure is not complete. These features



(a)



(b)

Figure 8: Impact of CZM parameters T_c (a) and G_c (b) on the quasi-static crack propagation for the linear elastic experimental case [2].

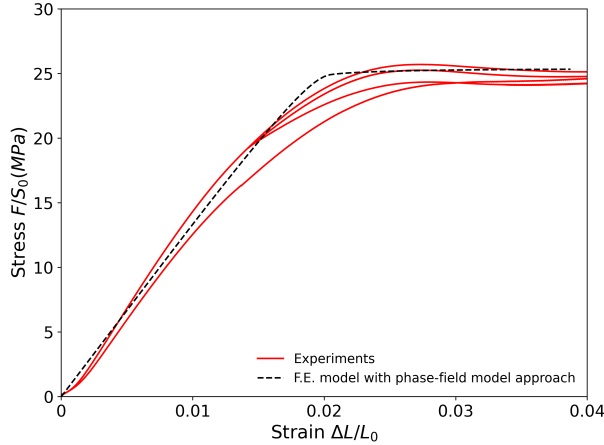


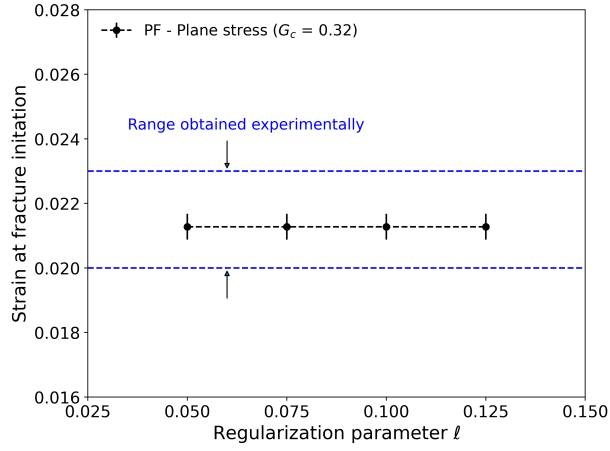
Figure 9: Comparison of the 2D plane stress macroscopic stress-strain response to the DCDC test experimental measures.

of incomplete damage process, localized plasticity, and smooth increase of the fracture energy are in agreement with the theoretical work [17] when plane stress assumptions are used. Note that when using the plane strain assumption, we have been able to reproduce the features displayed by [17, 41], with a crack progressing by jump and plasticity developing ahead of the crack, which is less representative of the experimental reality. Moreover, the numerical macroscopic stress-strain response overestimates significantly the experimental response.

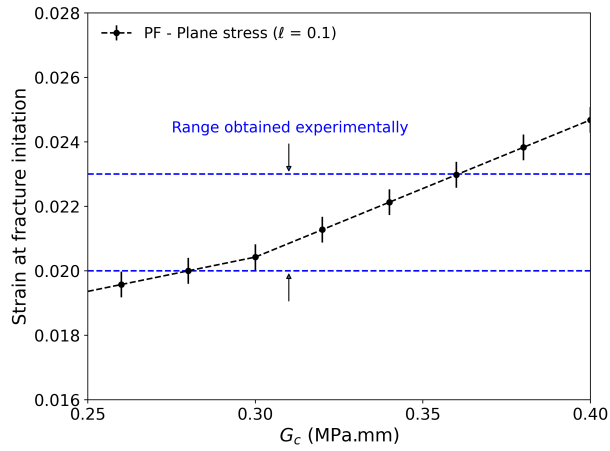
5.2 CZM results

The same steps have been applied as for the elastic case to choose the cohesive element mesh size and their initial stiffness K_0 , and in the end, values of 10 microns and $K_0 = 10000$ MPa/mm were retained. Unlike in the elasticity case, the elastic-perfectly plastic case produced convergence difficulties. This can be explained by the combination of small elements and small time steps required by the cohesive elements and possibly large deformation induced by plasticity. In the end, the compression was applied by displacement steps of $5 \cdot 10^{-4}$ mm in order to always observe crack initiation. However, note that depending on the cohesive element parameters T_c and G_c , the crack propagation could be witnessed or not, due to numerical divergence happening at early failure. Therefore, comparison with the crack propagation rate (Figure 4) could not be performed.

The range of tested values for T_c and G_c was chosen in order to always witness the plastic plateau on the macroscopic stress-strain curve before crack initiation, like for the experiments (Figure 3). Figure 14a shows the strain at failure with respect to the energy release rate G_c for a critical stress T_c equal



(a)



(b)

Figure 10: Macroscopic strain at damage initiation obtained using phase-field method (a) Impact of the regularization parameter ℓ at constant $G_c = 0.32$ MPa.mm and (b) dependence to the critical energy release rate G_c for $\ell = 0.1$ mm. The blue dashed lines indicate the range of experimental uncertainty defined by mean value and standard deviation.

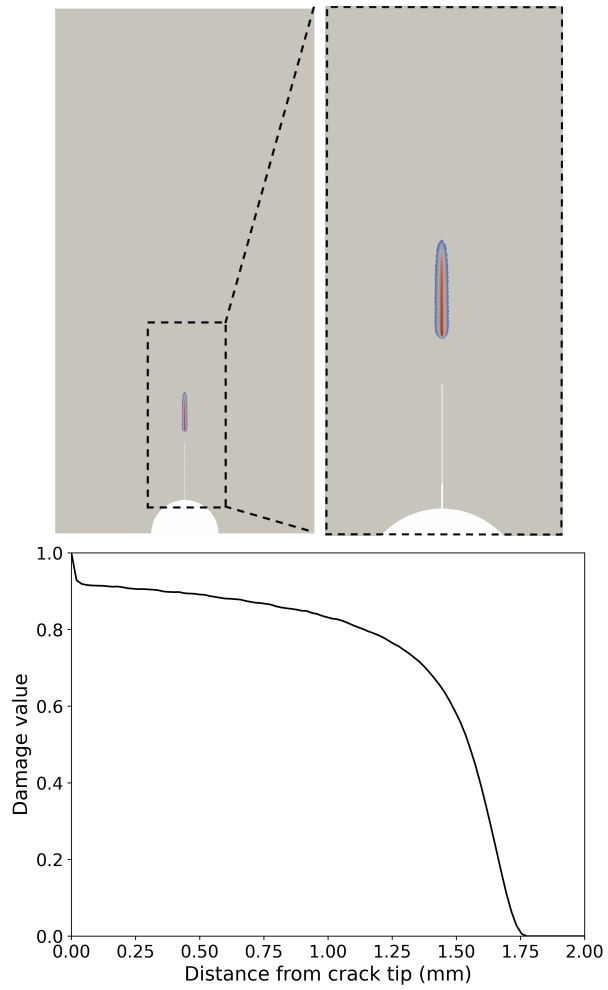


Figure 11: Diffuse damage field and damage value along the damaged area, obtained using phase-field method and plane stress assumptions.

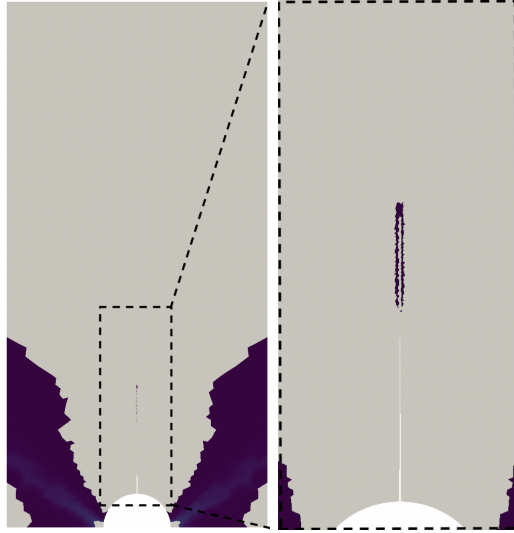


Figure 12: Cumulated plasticity in the specimen and along the crack during propagation, obtained using phase-field method and plane stress assumptions.

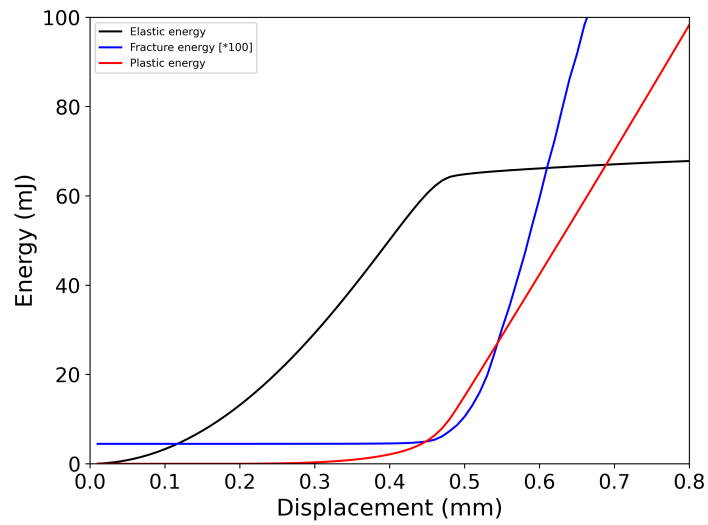


Figure 13: Energy changes with respect to the applied compressive displacement obtained with phase-field method

to the yield stress. The experiments are well reproduced for a reasonable and rather narrow range of values of $G_c \in [0.26, 0.32]$ MPa.mm. Setting G_c to 0.30 MPa.mm and varying the critical stress at crack initiation, one notes that T_c has no impact for values $T_c \in [29, 34]$ MPa. Consequently, the method seems adequate to reproduce the DCDC test and estimate the critical energy release rate of an elastoplastic material.

Both models have been able to reproduce the damage initiation at the experimentally observed macroscopic strain for ranges of values of G_c that overlap. Therefore, we can confidently estimate G_c at a value of 0.31 ± 0.03 MPa.mm. When reproducing our experimental data, the dependence of the phase-field results to ℓ was negligible, which probably explains that similar values of G_c were obtained for both phase-field and cohesive zone modeling.

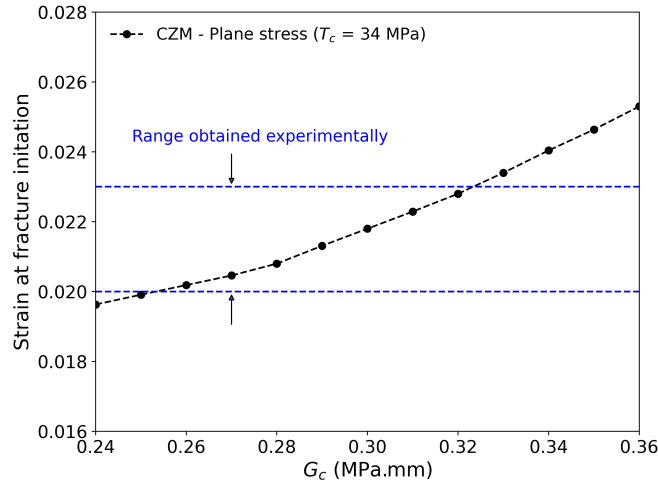
6 Conclusion

Double cleavage drilled compression may be applied to characterize material Mode I opening fracture. The critical energy release rate, G_c , may be simply evaluated by LEFM analysis when the material is linear elastic. To extend this test to elastoplastic materials, we have applied the phase-field approach to fracture and cohesive elements within a classic finite element framework. Both models have been compared to data from the literature in the context of linear elasticity, where G_c is known, and to original data obtained on an elastoplastic polymer.

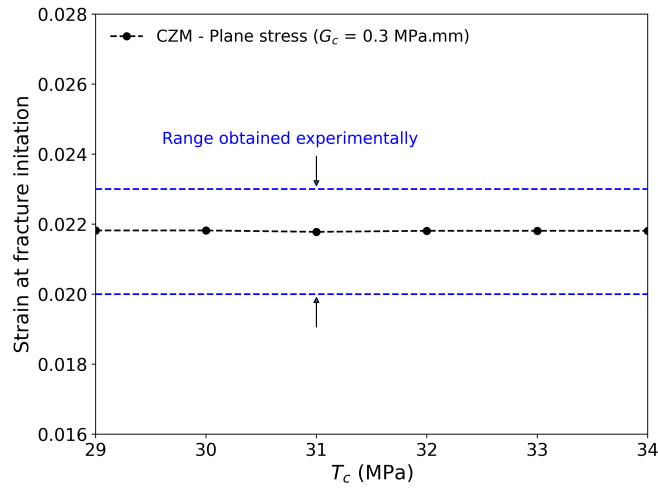
In linear elasticity, both damage models can reproduce fracture initiation at the experimentally observed macroscopic stress. However, the phase-field model has shown to be sensitive to the regularization parameter ℓ , and several values of G_c could be obtained according to the chosen value of ℓ . This parameter sensitivity has been discussed in the literature at large, and is very much dependent on the studied case. On the contrary, the cohesive zone model has shown little dependency on the strength T_c (within reasonable changes) and is therefore capable to retrieve the value of G_c provided by the LEFM analysis.

For the tested polymer, well approximated by an elastic-perfectly plastic behavior, the phase-field approach shows a macroscopic strain at crack initiation that was independent of ℓ (again within reasonable changes), which interestingly put all the model dependence on parameter G_c . Both models reproduced the experimental strain at fracture for similar ranges of values for G_c and a realistic value of G_c has been reached. However, the CZM approach has shown limitations in modeling the propagation of the crack in the context of elastic-perfectly plastic. Nevertheless, this remark cannot be generalized, since crack propagation was successfully observed when a single-edge notched bending test was similarly modeled.

In the end, this work has provided two possible fracture models to extract the critical energy release rate value resulting from a DCDC test run on an elastic-perfectly plastic material, extending the aforementioned test beyond the case of linear elastic materials.



(a)



(b)

Figure 14: Macroscopic strain at crack initiation obtained using CZM (a) with respect to the critical energy release rate G_c for critical stress $T_c = 34$ MPa and (b) according to the critical stress T_c value for $G_c = 0.30$ MPa.mm. The blue dashed lines indicate the range of experimental uncertainty defined by mean value and standard deviation.

Acknowledgement

The work is part of the Ph.D. of A. Coq supported by the Chair "Modelling advanced polymers for innovative material solutions" led by Ecole Polytechnique (l'X) and the Fondation de l'Ecole Polytechnique and sponsored by Arkema. Simulations were run on the Cholesky cluster from Ecole Polytechnique.

References

- [1] C. Janssen, in *Proc. 10th Int. Cong. On Glass* (Ceramic Society of Japan, Weinheim, Germany, 1974), pp. 10.23–10.30
- [2] T. Michalske, W. Smith, E. Chen, *Engineering Fracture Mechanics* **45**, 637 (1993)
- [3] M. He, M. Turner, A. Evans, *Acta Metallurgica Materialia* **84**, 104070 (1995)
- [4] T. Fett, G. Rizzi, D. Munz, *Engineering Fracture Mechanics* **72**, 145 (2005)
- [5] G. Pallares, L. Ponson, A. Grimaldi, M. George, G. Prevot, M. Ciccotti, *International Journal of Fracture* **156**, 11 (2009). DOI 10.1007/s10704-009-9341-8
- [6] Q. Wang, M. Ni, L. Wu, R. Huang, *Theoretical and Applied Fracture Mechanics* **96**, 803 (2018)
- [7] T. Nguyen, J. Yvonnet, M. Bornert, C. Chateau, K. Sab, R. Romani, R.L. Roy, *International Journal of Fracture*. **196**, 213 (2016)
- [8] C.G. Sammis, *Acta Metallurgica Materialia*. **34**, 511 (1986)
- [9] T. Plaisted, A. Amirkhizi, S. Nemat-Nasser, *International Journal of Fracture* **141**, 447 (2006). DOI 10.1007/s10704-006-9006-9
- [10] C. Nielsen, A.V. Amirkhizi, S. Nemat-Nasser, *Engineering Fracture Mechanics* **91**, 1 (2012). DOI 10.1016/j.engfracmech.2012.04.030
- [11] G.A. Francfort, J.J. Marigo, *Journal of the Mechanics and Physics of Solids* **46**, 1319 (1998)
- [12] B. Bourdin, G.A. Francfort, J.J. Marigo, *Journal of the Mechanics and Physics of Solids* **48**, 797 (2000)
- [13] K. Pham, K. Ravi-Chandar, C. Landis, *International Journal of Fracture* **205**, 83 (2017). DOI 10.1007/s10704-017-0185-3
- [14] E. Tanné, T. Li, B. Bourdin, J. Marigo, C. Maurini, *Journal of Mechanics and Physics of Solids* **10**, 80 (2018)

- [15] M. Ambati, T. Gerasimov, L. Lorenzis, *Computational Mechanics* **55**, 1017 (2015)
- [16] R. Alessi, M. Ambati, T. Gerasimov, S. Vidoli, L.D. Lorenzis, *Advances in Computational Plasticity* **46**, 1 (2018)
- [17] S. Brach, E. Tanné, B. Bourdin, K. Bhattacharya, *Computer Methods in Applied Mechanics and Engineering* **353**, 44 (2019)
- [18] J. Ulloa, J. Wambacq, R. Alessi, E. Samaniego, E. Degrande, G. François, *Journal of the Mechanics and Physics of Solids* **159**, 104684 (2022)
- [19] T. Nguyen, J. Yvonnet, D. Waldmann, Q. He, *International Journal for Numerical Methods in Engineering*, **121**, 4717 (2020)
- [20] V. Tvergaard, J.W. Hutchinson, *Journal of Mechanics and Physics of Solids* **41** (1993). DOI 10.1016/0022-5096(93)90057-M
- [21] M. Elices, G. Guinea, J. Gómez, J. Planas, *Engineering Fracture Mechanics* **69**, 137 (2002)
- [22] A. Turon, C. Dávila, P. Camanho, J. Costa, *Engineering Fracture Mechanics* **74**, 1665 (2007). DOI 10.1016/j.engfracmech.2006.08.025
- [23] M. Ortiz, A. Pandolfi, *International Journal for Numerical Methods in Engineering* **44**, 1267 (1999)
- [24] A. Doitrand, R. Estevez, D. Leguillon, *Theoretical and Applied Fracture Mechanics* **99**, 51 (2019). DOI 10.1016/j.tafmec.2018.11.007
- [25] D. Leguillon, *European Journal of Mechanics Solids/A* **21**, 61 (2002). DOI 10.1016/S0997-7538(01)01184-6
- [26] D. Yang, M. Bornert, S. Chanchole, H. Gharbi, P. Valli, B. Gatmiri, *International Journal of Rock Mechanics and Mining Sciences* **53**, 45 (2012)
- [27] H. Gharbi, W. Wenlong, C. Giraudet, J. Allain, E. Vennat. *Measure of the hygroscopic expansion of human dentin* (2022)
- [28] J. Schindelin, I. Arganda-Carreras, E. Frise, E. Kaynig, M. Longair, T. Pietzsch, S. Preibisch, C. Rueden, S. Saalfeld, B. Schmid, J.Y. Tinevez, D. White, V. Hartenstein, K. Eliceiri, P. Tomancak, A. Cardona, *Nature Methods* **72**, 676 (2012)
- [29] B. Bourdin, G.A. Francfort, J.J. Marigo, *Journal of elasticity* **91**, 5 (2008)
- [30] H. Amor, J.J. Marigo, C. Maurini, *Journal of the Mechanics and Physics of Solids* **57**, 1209 (2009)
- [31] C. Miehe, F. Welschinger, M. Hofacker, *International Journal for Numerical Methods in Engineering* **83**, 1273 (2010)

- [32] Z. Luo, L. Chen, N. Wang, B. Li, *Computational Mechanics* **70**, 931 (2022)
- [33] A. Kumar, B. Bourdin, G. Fracrot, O. Loez-Pamies, *Journal of the Mechanics and Physics of Solids* **142**, 104027 (2020)
- [34] L. de Lorenzis, C. Maurini, *International Journal of Fracture* **237**, 61 (2022). DOI 10.1007/s10704-021-00555-6
- [35] A. Logg, K.A. Mardal, G.N. Wells (eds.), *Automated Solution of Differential Equations by the Finite Element Method* (Springer, 2012)
- [36] C. Geuzaine, J.F. Remacle, *International Journal for Numerical Methods in Engineering* **79**, 1309 (2009)
- [37] S.V. Roberto Alessi, Jean-Jacques Marigo, *Archive for Rational Mechanics and Analysis* **214** (2), 575 (2014)
- [38] Abaqus, *SIMULIA Abaqus User Assistance* (Simulia, 2021)
- [39] A. Turon, C. Dávila, P. Camanho, J. Costa, *Engineering Fracture Mechanics* **74**, 1665 (2007)
- [40] S. Wiederhorn, H. Johnson, A. Diness, A. Heuer, *Journal of the American Ceramic Society* **57**, 336 (1974)
- [41] G.D. Maso, R. Toader, *Calculus of Variations and Partial Differential Equations* **59**, 1 (2020)